



Pressure-dependent bond stress-slip model for sand-coated FRP-concrete interface



Hongwei Lin, Peng Feng*, Jia-Qi Yang

The Key Laboratory of Civil Engineering Safety and Durability of China Education Ministry, Department of Civil Engineering, Tsinghua University, Beijing 100084, China

ARTICLE INFO

Keywords:

Concrete
Sand-coated
FRP profile
Interface
Bond stress-slip relationship

ABSTRACT

The natural bond between FRP (fiber reinforced polymer) profile and concrete is quite weak, additional measures for improving the FRP-concrete interface should be taken to ensure the hybrid FRP-concrete members work compositely. There are several methods for interface improvement, and this paper focuses on the sand-coating method. Experimental tests including pull-out tests and push-out tests were conducted on sand-coated FRP-concrete interface. Test results revealed that the interfacial behavior included two stages. In the first stage, the concrete surrounding the plate failed in shear, which was similar to the adhesive bonding FRP-concrete interface. In the second stage, interfacial dilatation was induced and significant friction took place between fractured concrete surfaces. The adhesive-FRP interface and adhesive-sand aggregates interface were further damaged. Based on test results and numerical analysis, the variation of the interfacial dilatation and friction coefficient with the interfacial slip were determined. Finally, a pressure-dependent bond stress-slip model which was suitable for both active and passive confinement conditions was developed. This model can be implemented into commercial FE software and used for FE analysis of structural members. Comparisons with test results of the present paper and those from the literature indicate that the proposed model can provide reliable predictions.

1. Introduction

Corrosion has become a global problem that threatens the safety and service life of traditional structures. Considerable economic costs are generated for the maintenance, repair and rehabilitation of corrosion damaged structures. The statistics reported in China, Europe and North America indicate that the economic loss associated with corrosion is worth billions of US dollars for a single year [1–5]. To eliminate the corrosion problem, fiber reinforced polymer (FRP) composites are increasingly used as a promising alternative of steel in the construction domain. They have many advantages including high strength and stiffness, good resistance to chemical agents, light weight and ease of installation, etc. Among the FRP composites of different forms, pultruded profiles resembling steel profiles have been widely used. With FRP profiles as the main components, a number of innovative steel-free structural hybrid FRP-concrete columns have been developed [6,7]. A typical example is the one recently developed in Tsinghua University for marine construction [8], see Fig. 1. This column consists of a concrete-filled FRP tube (CFFT) longitudinally reinforced with a number of pultruded FRP profiles in a direct contact with the FRP

tube. It is denoted as pultruded profile-reinforced CFFT (PPR-CFFT) column. The FRP tube is used for providing lateral confinement to the inner concrete [9], and the pultruded FRP profiles are introduced to enhance the bending resistance.

To ensure the superior performance of the hybrid column under various loading conditions, adequate composite action between the concrete and the FRP profiles is especially important. A parallel study by Wang [8] demonstrated that the PPR-CFFT column with perforated FRP profiles showed much better mechanical performance over the control specimen when subjected to combined axial compression and bending. Therefore, the FRP-concrete interface is of great importance. The natural bond between FRP profile and the concrete cannot meet requirements because the surface of FRP profiles is very smooth [10,11]. In view of this, several methods have been proposed by researchers to improve FRP-concrete interface. These methods can be categorized into two types: (1) adhesive bonding, including wet-bonding [12–15], sand-coating [16–18], shear-key bonding [19,20], etc. (2) mechanical interlock, including steel bolt connection [21–25], FRP bolt connection [26–28], concrete dowel interlock [29–31], composite dowel interlock [32,33], etc. The present study

* Corresponding author.

E-mail address: fengpeng@tsinghua.edu.cn (P. Feng).

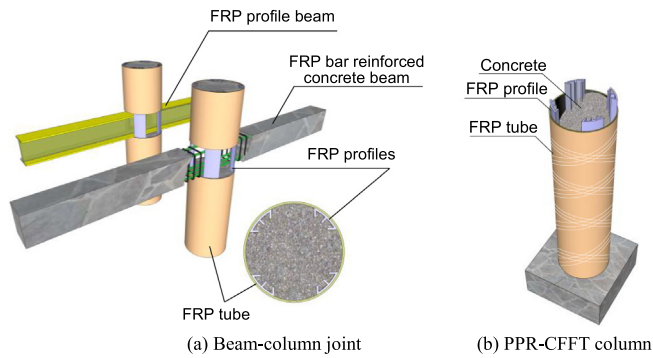


Fig. 1. Schematic illustration of the proposed hybrid column and joint.

focuses on the interfacial properties of sand-coated FRP-concrete interface.

For the past thirty years, there are numerous studies on the FRP-concrete bond problems. A majority of these studies are centered on the externally bonded reinforcement (EBR) and the near-surface mounted (NSM) techniques, both of which are for strengthening purposes and are adhesive-based. The sand-coating method, which is suitable for FRP profile-fresh concrete interface, is less studied. Among the scattered studies in the literature, the sand-coating method is mainly used for new bridge deck systems made of FRP open forms and concrete. It was found that the sand-coated interface could ensure the FRP section and concrete work compositely. Compared with the mechanical interlock methods, the sand-coating method can provide better bending properties. Experimental tests revealed that the possible failure modes of sand-coated interface included FRP-adhesive interface failure and concrete cohesive failure, both of which are brittle in nature. Goyal et al. [18] pointed out that the bonding performance of sand-coating and wet-bonding were comparable. This has been confirmed by other test results [17]. Systematic studies on the sand-coated interface were performed by Cho et al. [16,34]. They found that the failure of sand-coated interface could occur in the concrete or the adhesive depending on the distribution density and the aggregate size. A mixed failure mode might be observed. It was concluded that smaller aggregate size and larger distribution density could lead to better shear performance. However, excessively small aggregate size would compromise the bonding performance in the normal direction. Bilinear bond stress-slip models based on specific results of shear bond tests were derived as well. Experimental findings by Cho et al. [35] further revealed that the freezing-thawing cycles could hardly affect the bond performance of sand-coated interface.

A summary of the above mentioned studies show that the sand-coating method can well improve the FRP-concrete interfacial behavior. However, none of those studies involves lateral confinement, which is a critical factor for FRP-concrete hybrid columns. As schematically shown in Fig. 2, the lateral confinement results in the transverse pressure at the FRP-concrete interface. According to former studies on adhesive-bonding FRP sheet/plate-concrete interface, the lateral compression could significantly change the interfacial behavior. In order to solve the premature debonding problem, researchers proposed to induce lateral compression at the adhesive-based interface through measures such as U-jacketing [36,37], mechanical fasteners [38,39] and active compression [40,41]. Based on the test results of double-lap shear tests, Biscaia et al. [40,41] proposed a bond stress-slip model for the GFRP-concrete interface under external compression. The bond model was derived by further superimposing the frictional component on the basis of bond model for cases with no compression. A similar methodology was adopted by Lee and Lopez [36], in which a frictional bond stress-slip model for the concrete-FRP interface with U-shape wrapping was proposed. Assuming that the bond behavior of FRP-

concrete adhesive interface with mechanical fasteners shares some similarities with internal reinforcing bars, Wu and Liu [39] developed an analytical bond stress-slip model for HB-FRP joints. Even though these models have considered the influence of lateral pressure on bond-slip behavior, they are only suitable for certain confinement conditions. The adopted assumption of constant frictional bond stress is not substantiated as well.

To address the above mentioned research gaps, the present study casts a deep insight into the mechanical behavior of sand-coated interface with lateral confinement. Based on test results and numerical analysis, the influence of lateral pressure on the interfacial behavior is systematically analyzed and a general bond stress-slip model applicable for various confinement conditions is proposed.

2. Experimental studies

2.1. Test specimens

The pull-out and push-out test methods were used to examine the interfacial behavior between the sand-coated FRP profiles and concrete. The test samples included a concrete cylinder with GFRP plate centrally embedded. The concrete block was confined by a GFRP tube with an inner diameter of 200 mm and an averaged thickness of 4.5 mm. The GFRP plate was 101.6 mm in width and 650 mm in length. Both sides of the plate were coated with coarse silica sand aggregates, which had an average diameter of 5–10 mm. The intended bonding surface of the GFRP plate was firstly coarsened by belt sander to improve bonding. Sand aggregates were then bonded to the plate with a 1.0 mm thick layer of Lica-131A/B adhesive. The tested tensile strength and elastic modulus of the adhesive were 45 MPa and 7.2 GPa, respectively. For each side of coated interface, a density of 0.59 g/cm² coarse silica sand aggregates were used. Fig. 3 shows the sand-coated interface. After the complete hardening of the adhesive, the plate was put into the tube and the concrete was then cast.

Originally, the height of all the specimens was 300 mm and the bond length between the plate and the concrete was 250 mm. However, due to the presence of GFRP tube, the interfacial resistance of FRP profile was quite large. Initial trial tests indicated that the specimens failed at the load end before the plate was pulled out. The long bond length specimens were therefore cut into short bond length specimens. The remaining specimens and the removed ones were subjected to pull-out and push-out loading, respectively. For the pullout specimens, an unbond length of 50 mm was set via two foam blocks. In total, 7 specimens were fabricated and their information is listed in Table 1. Fig. 4 illustrates the geometrical configurations of the specimens.

2.2. Material properties

2.2.1. Concrete

All the specimens were cast from the same batch of concrete prepared in the laboratory. The coarse aggregate was crushed limestone with a maximum size of 15 mm. The average compressive strength measured on cubes (150 mm × 150 mm × 150 mm) and prisms (150 mm × 150 mm × 300 mm) at the time of loading tests were 45.7 MPa and 32.7 MPa, respectively.

2.2.2. GFRP tube

The GFRP tubes were fabricated using the filament-winding method and were composed of E-glass fibers and epoxy resin with a fiber volume fraction of 75%. The fibers were oriented at ± 85° with respect to the longitudinal axis of the tubes. The mechanical properties of the tube were tested by the manufacture. The longitudinal tensile strength was 41 MPa, while the hoop tensile strength was 695 MPa. The hoop elastic modulus was 32.7 GPa.

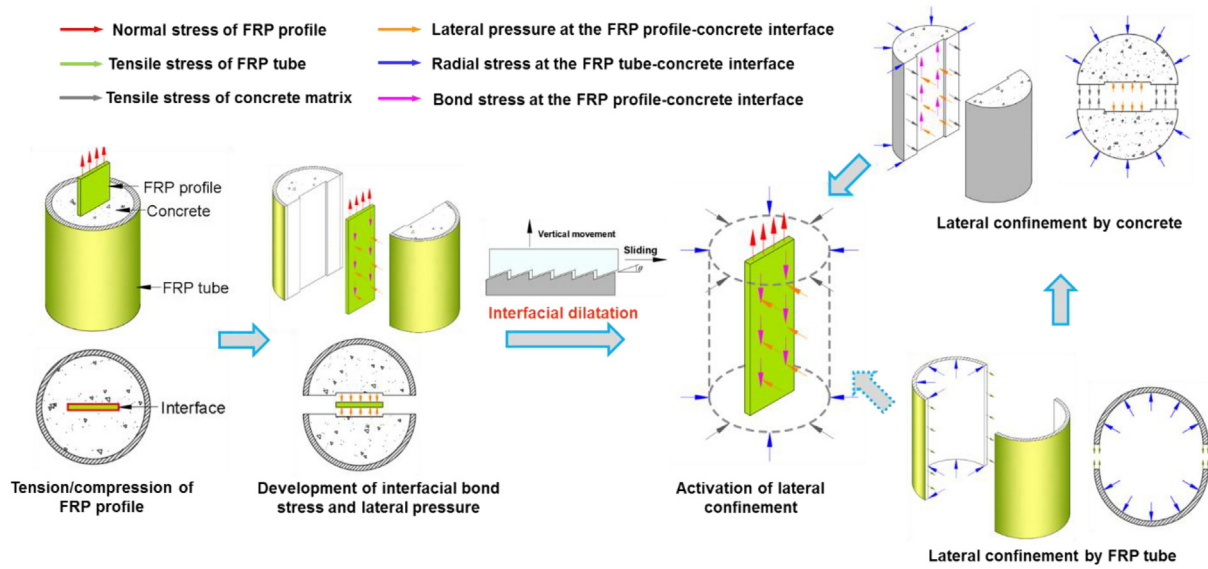


Fig. 2. Schematic illustration of the FRP-concrete interface with hoop confinement.

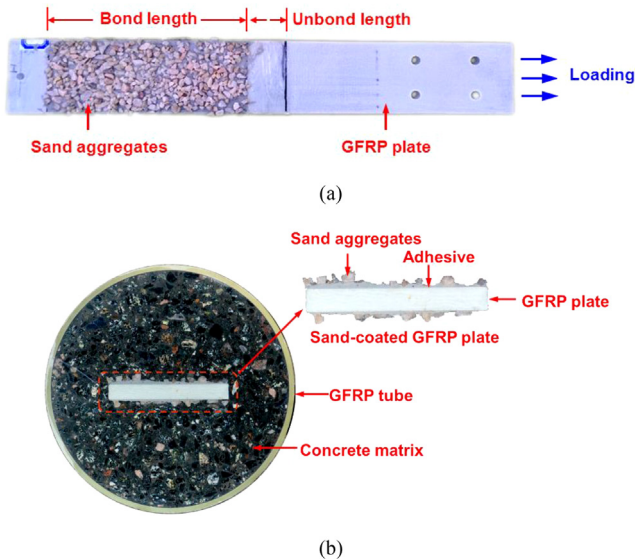


Fig. 3. Sand-coated FRP-concrete interface (pull-out specimen): (a) sand-coated FRP plate; (b) cross-section.

2.2.3. GFRP plate

The GFRP plates, produced by Nanjing Spare Composites Co Ltd, were all 650 mm in length, 101.6 mm in width, and 12.7 mm in thickness. The plates were made of E-glass fibers and a polyethylene resin matrix and manufactured by a pultrusion technology. The mechanical

properties of the pultruded plate were experimentally determined by the manufacture, as listed in Table 2.

2.3. Test setup and instrumentation

Fig. 5 shows the test setup. The specimens were all monotonically tested. For the pull-out loading, a hinged connection was adopted between the testing machine and the GFRP plate in order to reduce the bending effect. The upward load was applied to the GFRP plate under displacement-control with a constant rate of 0.4 mm/min. The movement of the concrete block was restrained by a specially designed loading frame. Both at the free end and loaded end of each specimen, two linear variable displacement transformers (LVDTs) were respectively installed to measure the relative slips between GFRP plate and concrete. For the push-out loading, a “T” shaped steel angle was used to transfer the load of universal testing machine to the GFRP plate. The specimen was supported at the free end by a bespoke reaction frame. Two LVDTs were used to monitor the free end slips.

Hoop strains of the GFRP tube were measured using strain gauges. Considering the hoop strain of the tube might not be the same along the vertical direction, the strain gauges of long bond length specimen L-250-PL were positioned at the locations of 60 mm, 125 mm, and 190 mm from the bottom of the specimen. At each height, there were four strain gauges, 90-degree apart. For the short bond length specimens including S-100 and S-50 specimens, only four strain gauges were adopted. The longitudinal and circumferential layouts of the strain gauges are shown in Fig. 6. All test data, including the strains, loads, and displacements, were automatically recorded by a computer-aided data acquisition system.

Table 1
Test specimen matrix.

Designation	Height (mm)	Bond length (mm)	Unbond length (mm)	Loading method
L-250-PL	300	250	50	Pull-out
S-100-PL-1	150	100	50	Pull-out
S-100-PL-2	150	100	50	Pull-out
S-100-PL-3	150	100	50	Pull-out
S-50-PS-1	50	50	–	Push-out
S-100-PS-2	100	100	–	Push-out
S-100-PS-3	100	100	–	Push-out

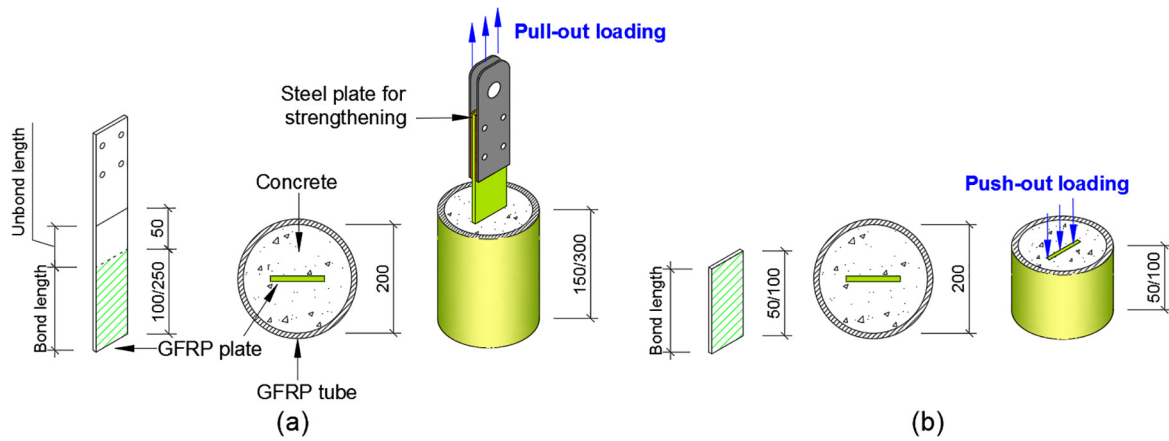


Fig. 4. Geometric configurations of (a) the pull-out and (b) push-out specimens (all dimensions are in mm).

Table 2
Mechanical properties of the GFRP plates.

Thickness	Longitudinal direction					Transverse direction	
	Strength (MPa)			Young's modulus (GPa)		Compressive	
	Tensile	Compressive	In-plane shear	Tensile	Compressive	Strength (MPa)	Young's modulus (GPa)
12.7 mm	531	377	32.3	33.2	24	108.3	11.2
6.35 mm	524	387	32.1	31.1	21.7	113.3	12

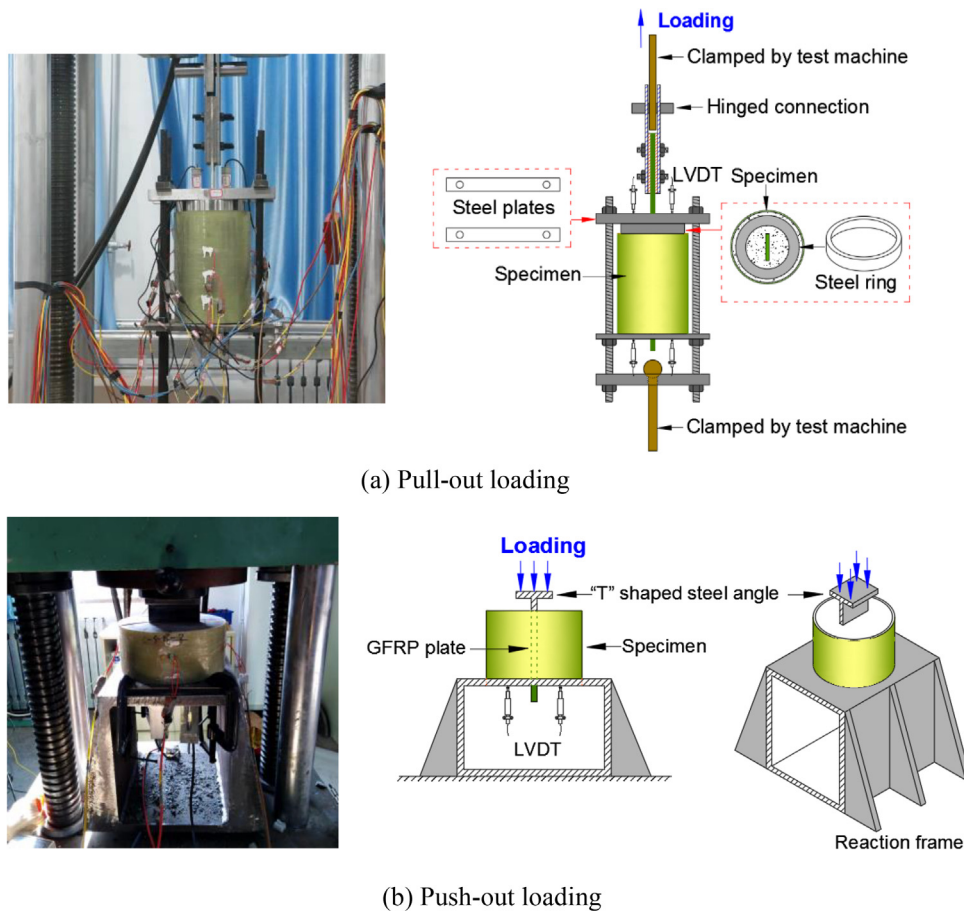


Fig. 5. Pull-out and push-out test setup.

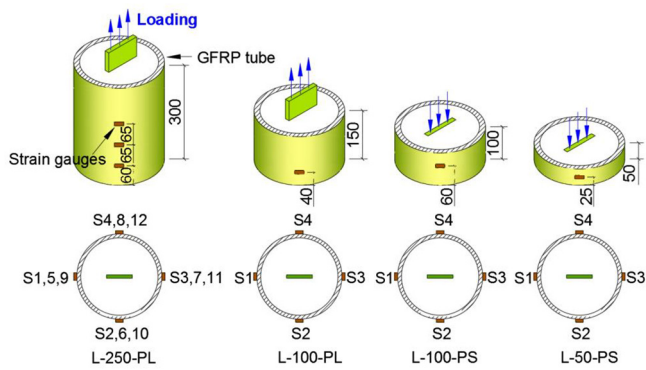


Fig. 6. Longitudinal and circumferential layouts of the strain gauges.

2.4. Test results

2.4.1. Pull-out specimens

The only long bond length specimen L-250-PL failed drastically by clamping failure at the loading end. The desired interfacial failure between the FRP plate and concrete did not occur. The clamping failure at the loading end was characterized by the shear-out failure of GFRP plate and debonding failure between the GFRP plate and steel plates. In the following analysis, the tested data is only used for verification purpose. The short bond length specimens all failed at the FRP-concrete interface, see Fig. 7. At the load end of the bond zone, a cluster of concrete attaching on the FRP profile was observed. At the free end of the bond zone, the sand and adhesive were completely lost due to abrasion. This indicates that the failure firstly occurred in the concrete surrounding the plate. Then the friction between the crushed concrete and the surrounding concrete took place. The significant friction at the interface further damaged the sand-adhesive interface and the plate-adhesive interface. As the free end experienced the most slip, the interfacial damage was more severe.

Fig. 8 shows the measured load-slip curve and the hoop strain developments of specimen L-250-PL. The tested maximum load was 342.6 kN. Before the final plate failure, the free-end slip was hardly developed, while continuous increase of the load-end slip was observed since the load level of around 100 kN. When the load reached about 327 kN, it plateaued and increased again until the final failure. The load plateau is believed to be caused by progressive load-end anchorage failure and not associated with interfacial behavior.

For the short bond length specimens, it is assumed that the bond length is short enough to result in a local bond behavior. The rationality of the assumption will be further discussed in the following section. With this assumption, the bond stress is averaged along the bond length. Fig. 9 shows the tested average bond stress-slip curves and

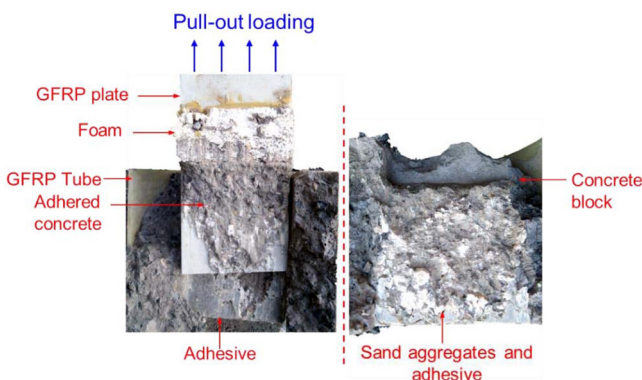


Fig. 7. Interfacial failure mode of pull-out specimens.

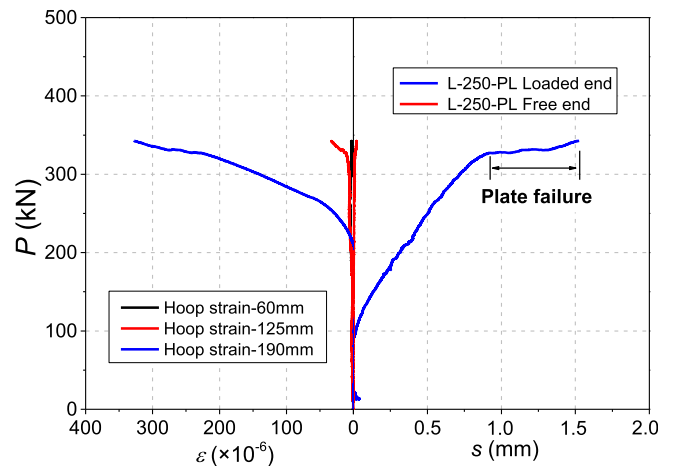


Fig. 8. Load-slip curves of long bond length specimen.

the hoop strain developments. The bond stress increases sharply in the ascending branch and yields near the peak. After the peak, the bond stress decreases gradually with the increase of interfacial slip. An apparent residual branch can be noticed. Compared with previous studies on FRP-concrete interface, in which no lateral confinement is involved, the tested interfacial behavior in the present study is much more ductile.

2.4.2. Push-out specimens

The failure mode of push-out specimens was the same as pull-out specimens. As shown in Fig. 10, the interfacial damage was more apparent at the load end. The adhesive together with the sand were completely removed from FRP plate. Part of the adhesive was attached on the surrounding concrete forming a smooth surface. At the free end, the bonding between the adhesive and the FRP plate is relatively intact. However, apparent abrasion can be noticed. The reason for this phenomenon is that the load end experienced more slip and more significant friction, while the free end experienced less slip due to push-out.

Fig. 11 shows the average bond stress-slip curves and the hoop strain developments of push-out specimens. Compared with the pull-out specimens, the tested interfacial strength of push-out specimens is slightly larger. Apart from the specimen S-S-PS1, the bond-slip curves under push-out loading are similar to those under pull-out loading. The abnormal load-slip behavior of specimen S-50-PS-1 is due to experimental errors associated with rigid motion, and therefore the test data of S-50-PS-1 is excluded in the following analysis.

3. Discussions

3.1. Bond-slip mechanism

As introduced above, the interfacial failure of the FRP-concrete interface is initially characterized by concrete cracking adjacent to the adhesive layer, which is quite similar to that of externally bonded FRP joints. After that significant friction takes place between the crushed concrete adhering to the plate and the surrounding concrete. The all-stage interfacial behavior is schematically illustrated in Fig. 12. In the early stage of loading, i.e. stage I, extensive cracks are gradually developed in the concrete matrix and the lateral confinement is hardly activated. In stage II, the friction between the fractured concrete surfaces takes place. As the fractured surfaces are microscopically rough, any sliding between the fractured concrete surfaces will result in an opening (dilatation) in the lateral direction. The dilatation of concrete block will consequently activate the lateral confinement of GFRP tube.

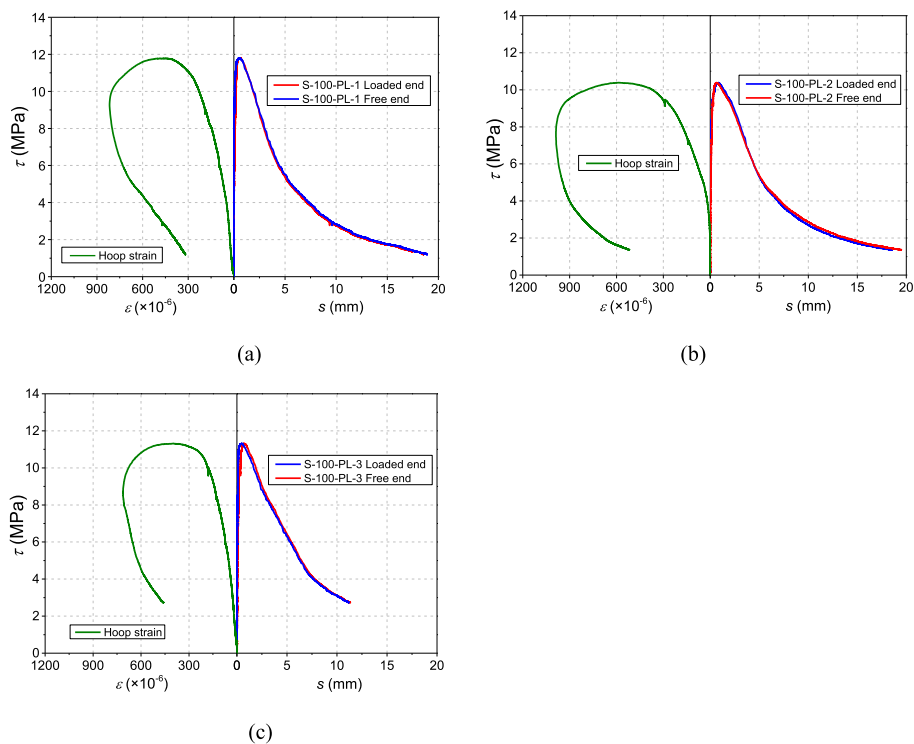


Fig. 9. Average bond stress-slip curves of pull-out specimens.

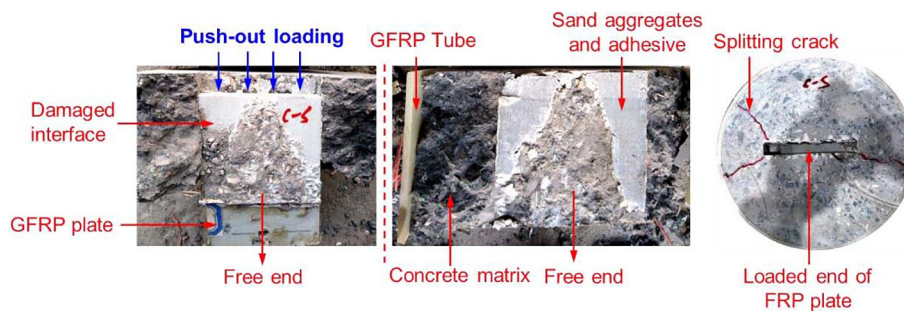


Fig. 10. Interfacial failure mode of push-out specimen (specimen S-100-PS-2).

The maximum hoop strain of GFRP tube appears slightly later than the peak shear stress. After the peak, the hoop strain shows a phenomenon of retraction and keeps a residual value at the final stage. Similar phenomenon has been observed in steel–concrete bond problems [42].

3.2. Short bond length assumption

As the tested slips at the load end and the free end are very close, it is assumed that the bond length is short enough to result in a local bond behavior. To verify this assumption, a 3-dimensional finite element model of pull-out specimen with a short bond length was created utilizing the commercial software ABAQUS [43], see Fig. 13(a). The concrete block and the FRP plate were meshed with solid elements C3D8R. The FRP jacket was meshed with shell elements S4R. The steel–concrete interface was modeled by 8-node cohesive elements (COH3D8) with a thickness of 1.0 mm. The tested bond stress-slip curve of specimen S-100-PL-1 (the slip is the average of loaded end and free end slips) was used for determining the damage evolution. Concrete damage plasticity model in ABAQUS [43] was adopted to model the concrete block. The FRP plate and FRP tube were all mod-

eled as elastic material. The calculated and tested bond stress-slip curves are compared in Fig. 13(b). It can be seen that the average bond stress-slip curve by FE analysis almost overlaps with the tested curve. The prerequisite for this phenomenon is that the bond length is very short, otherwise considerable difference will be observed between the input and output bond stress-slip curve. Therefore, the average bond stress-slip curves are very close to the local bond behavior. This further reveals that a short bond length might be more proper for an experimentally investigated case of FRP-concrete interface with lateral confinement. This is similar to steel–concrete bond problems, for which a very short bond length is usually adopted. Generally, for bond problems of the externally bonded FRP plate/sheet, a very long bond length is required. However, this is no longer suitable for this study. A very long bond length may cause extreme difficulties for the loading tests. Therefore, great care should be taken in designing FRP-concrete interface related experiments. The optimized short bond length might have a close relationship with FRP plate stiffness, sand-coating properties and properties of surrounding concrete, but it is beyond the scope of the present paper. The finding in this study can provide references for future studies.

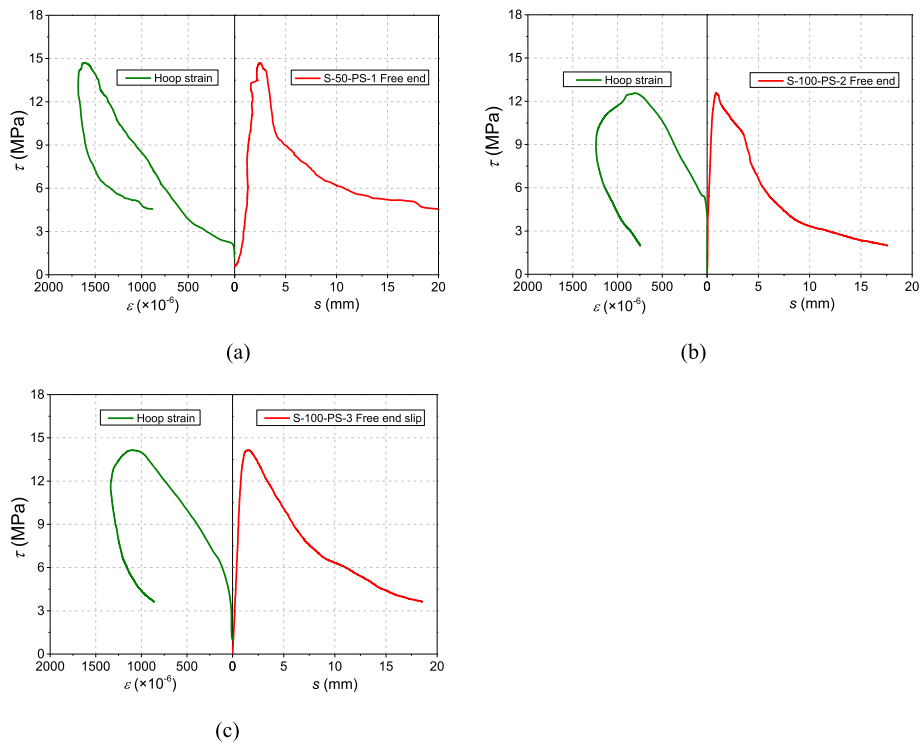


Fig. 11. Average bond stress-slip curves of push-out specimens.

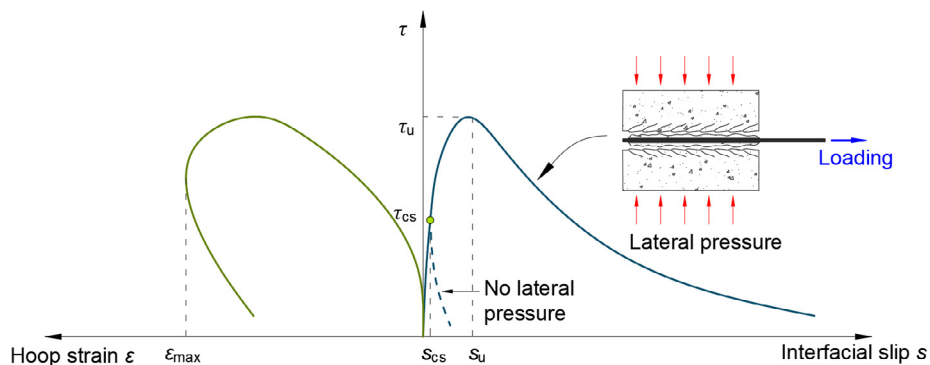


Fig. 12. Bond-slip mechanism of FRP-concrete interface with lateral pressure.

3.3. Comparisons with existing models

In the initial stage when the confinement of GFRP tube is hardly activated, the tested bond stress-slip curves in this study show similarities with those of externally bonded FRP joints. Typical bond stress-slip models for externally bonded (EB) FRP joints are therefore selected for comparisons. Until now, numerous models for EB joints have been proposed. Among the models, the models proposed by Nakaba et al. [44], Dai et al. [45], and Lu et al. [46] have been widely accepted by researchers. The model by Nakaba et al. [44] is experimentally determined based on closely spaced strain gauges, while the model by Dai et al. [45] is experimentally determined based on the load end force-displacement curves. Lu et al. [46] developed their model based on meso-scale finite element analysis. These three models are listed in Table 3. Comparisons between the model predictions and the tested curves are shown in Fig. 14. All these three models agree very well with the ascending branches of the tested curves. This further justify the above conclusion that the interfacial behavior of

sand-coated FRP plate is initially close to that of EB joint. The critical point where the friction between fractured concrete surfaces exactly comes into being is very difficult to be determined, because the concrete cracking at the interface is a gradual and continuous process. It is certain that the friction takes place before reaching the shear strength τ_{cs} , which is the peak bond stress of EB joint. For simplicity, τ_{cs} is taken as the critical point where the friction mechanism is initiated.

4. Model development

4.1. Determination of the bond stress in stage I

In stage I, the shear resistance is primarily provided by concrete. As shown in Fig. 14, the interfacial behavior in stage I can be well predicted by existing models in Table 3. The continuous model proposed by Dai et al. [45] is slightly modified and adopted in this study,

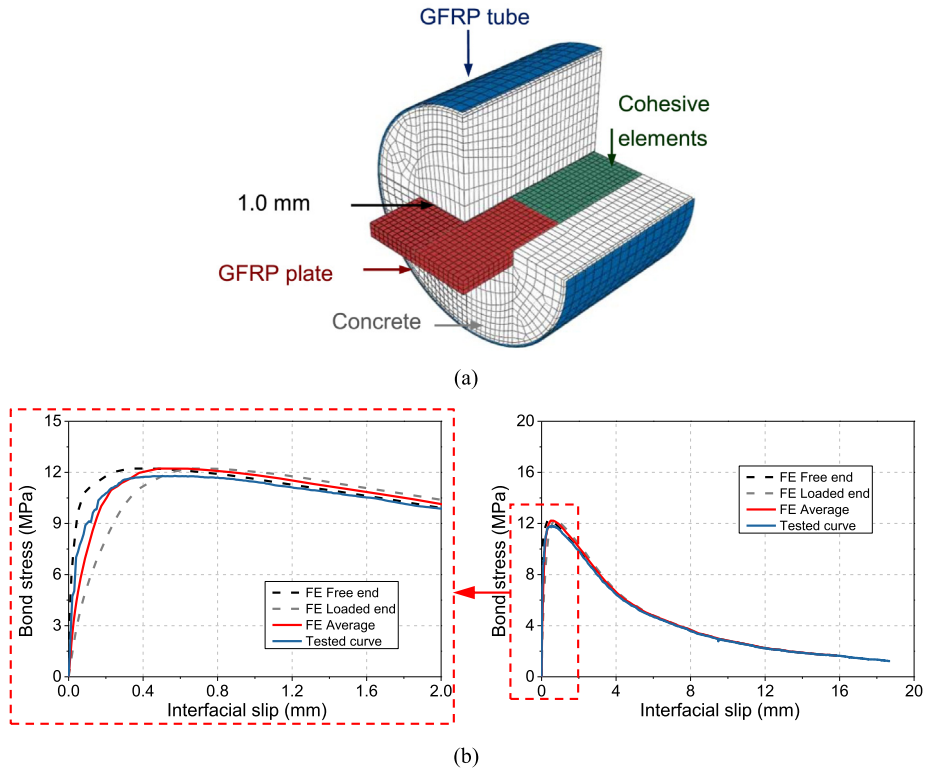


Fig. 13. Simulation of pull-out specimen with short bond length: (a) FE model; (b) comparison between tested and calculated curves.

Table 3
Models for bond stress-slip behavior of EB FRP joints in the literature.

Reference	Model expression	Key parameters
Nakaba et al. [44]	$\frac{\tau}{\tau_{\max}} = \frac{s}{s_0} \frac{n}{(n-1) + (\frac{s}{s_0})^n}$	$\tau_{\max} = 3.5f_c^{0.19}, s_0 = 0.065\text{mm}, n = 3.$
Dai et al. [45]	$\tau = 2BG_f(e^{-Bs} - e^{-2Bs})$	$\tau_{\max} = 0.5BG_f, s_0 = 0.693/B, B = 6.846(E_f t_f)^{0.108} (G_a/t_a)^{0.833}, G_f = 0.446(E_f t_f)^{0.023} (G_a/t_a)^{-0.352} f_c^{0.236}$
Lu et al. [46] (Simplified)	$\tau = \begin{cases} \tau_{\max} \sqrt{\frac{s}{s_0}} & (s \leq s_0) \\ \tau_{\max} e^{-\alpha(\frac{s}{s_0}-1)} & (s > s_0) \end{cases}$	$\tau_{\max} = \alpha_1 \beta_w f_t, \beta_w = \sqrt{\frac{2.25-b_f/b_c}{1.25+b_f/b_c}}, s_0 = 0.0195\beta_w f_t, \alpha = \frac{1}{\frac{\tau_f}{\tau_{\max s_0}} - 3}, G_f = 0.308\beta_w^2 \sqrt{f_t}$

where τ is the local bond stress; s is the local slip; τ_{\max} is the peak bond stress; s_0 is the local slip at τ_{\max} ; f_c is the concrete compressive cylinder strength.

where E_f and t_f is the elastic modulus and thickness of the FRP sheets; G_a is the shear modulus of adhesive layer; t_a is the thickness of adhesive layer.

where b_c is the width of concrete prism; b_f is the width of FRP plate; G_f is the interfacial fracture energy; f_t is the concrete tensile strength; $\alpha_1 = 1.5$.

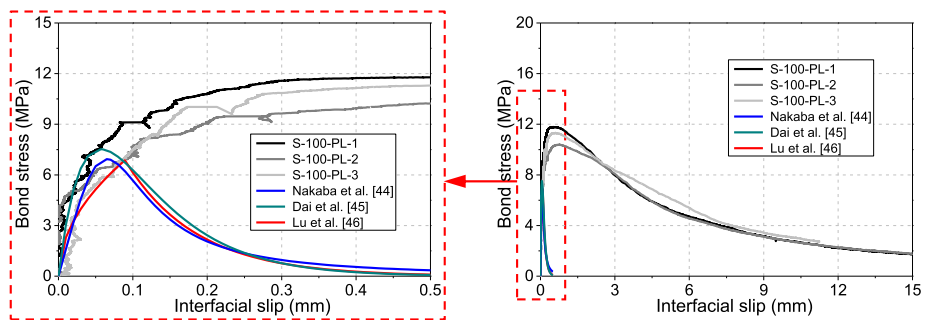


Fig. 14. Comparisons between tested curves and models for EB joints in the literature.

$$\tau(s) = \tau_c(s) \tag{1}$$

$$\tau_c(s) = 4\tau_{cs}(e^{-k_{cs}s} - e^{-2k_{cs}s}) \tag{2}$$

where $\tau_c(s)$ is the shear contribution of concrete; τ_{cs} is the maximum bond stress in stage I. For the determination of τ_{cs} , the model by Lu et al. [46] is suggested. Adhesive with high shear stiffness and

strength is suggested for sand-coated interface, and the parameter k_{cs} is simplified to $k_{cs} = 6.32(E_f t_f)^{0.108}$. The corresponding slip of τ_{cs} is defined as s_{cs} , after which the interfacial dilatation starts coming into effect. According to Dai et al. [45], $s_{cs} = 0.693/k_{cs}$.

4.2. Determination of the bond stress in stage II

In stage II, the interfacial dilatation induces pressure at the interface due to the lateral confinement. Consequently, the interfacial friction is generated when horizontal sliding occurs. The bond stress in stage II includes two components,

$$\tau(s) = \tau_c(s) + \tau_f(s) \tag{3}$$

where $\tau_f(s)$ is the shear contribution of the interfacial friction.

4.2.1. Tested friction component

With the tested bond stress-slip curves, the friction component of each specimen can be obtained by deducting the shear contribution of concrete (Eq. (3)). Fig. 15 shows the development of the friction component of each specimen.

4.2.2. Theoretical model for friction component

The interfacial friction is closely related to the interfacial pressure. To determine the developments of the interfacial pressure when the FRP plate is gradually pulled/pushed out of the concrete matrix, 3D FE models simulating the interfacial dilatation of pullout specimens were created by ABAQUS. According to the symmetry conditions, only a quarter of the pullout specimen was modeled, see Fig. 16. The concrete was meshed with solid elements C3D8R. The FRP jacket was meshed with 4-node quadrilateral membrane elements M3D4R and treated as a linear elastic brittle material. To ensure that the FRP jacket only provide strength and stiffness in the hoop direction, the Poisson's ratio was set to zero. The interaction between FRP tube and concrete was set as a parameter and its influence on the numerical results was investigated.

The Concrete Damage Plasticity (CDP) model provided by ABAQUS [43] has been widely used by researchers to model the concrete properties. The yield criterion of CDP model is based on the work by Lubliner et al. [47] and Lee and Fenves [48]. It is determined by parameters like the strength ratio of concrete under equal biaxial compression to uniaxial compression, and the strength ratio of concrete under equal biaxial compression to triaxial compression. The CDP model assumes a non-associated flow rule, and the Drucker-Prager hyperbolic function is utilized as the flow potential. Generally, good numerical results can be obtained with CDP model. However, CDP model has its limitations when it is used for the simulations of actively and passively confined concrete. It is pointed out by Yu et al. [49,50] that the hardening/softening rule, the flow rule and the damage variable should be confinement-dependent. In view of this, modifications to the CDP model was made by Yu et al. [49,50]. The modifications were

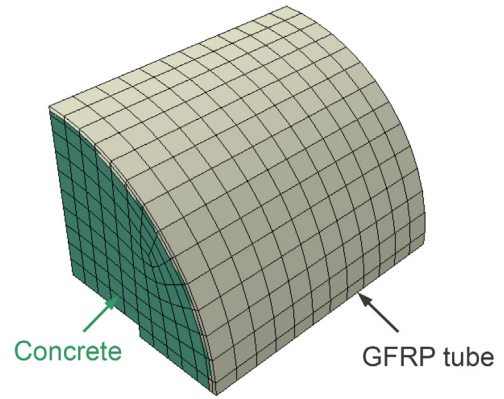


Fig. 16. 3D FE model for the simulation of interfacial dilatation.

implemented into ABAQUS using the user defined subroutine USDFLD. The modified CDP model (MCDP) can provide close predictions of the behavior of both actively-confined and FRP-confined concrete. In this paper, the concrete block is passively confined by FRP tube. Therefore, the modified CDP model by Yu et al. [49,50] was adopted. The influence of concrete model on numerical results was discussed in the following section. In the implementation of MCDP model, the stress-strain data for concrete under compression is generated based on the following equations,

$$\frac{\sigma_c}{f_{cc}^*} = \frac{(\epsilon_c/\epsilon_{cc}^*)^r}{r - 1 + (\epsilon_c/\epsilon_{cc}^*)^r} \tag{4}$$

$$r = \frac{E_c}{E_c - f_{cc}^*/\epsilon_{cc}^*} \tag{5}$$

$$\frac{f_{cc}^*}{f_{co}^*} = 1 + A_1 \left(\frac{\sigma_1}{f_{co}^*} \right)^{A_2} \tag{6}$$

$$\frac{\epsilon_{cc}^*}{\epsilon_{co}^*} = 1 + B_1 \left(\frac{\sigma_1}{f_{co}^*} \right)^{B_2} \tag{7}$$

where σ_c and ϵ_c are the axial stress and the axial strain; f_{cc}^* and ϵ_{cc}^* are the peak axial stress and the corresponding axial strain; f_{co}^* and ϵ_{co}^* are the compressive strength of unconfined concrete and the corresponding axial strain, $f_{co}^* = 36.56\text{MPa}$, $\epsilon_{co}^* = 0.000937\sqrt[4]{f_{co}^*}$; E_c is the elastic modulus of concrete, $E_c = 4730\sqrt{f_{co}^*}$; σ_1 is the confining pressure; A_1 , A_2 , B_1 , and B_2 are empirical coefficients. According to Teng et al. [51], $A_1 = 3.5$, $A_2 = 1.0$, $B_1 = 17.5$, and $B_2 = 1.0$. A recent study by Yang and Feng [9] indicates that parameters $A_1 = 3.33$, $A_2 = 0.90$, $B_1 = 17.4$, and $B_2 = 1.07$ can lead to improved estimations for heavily confined conditions.

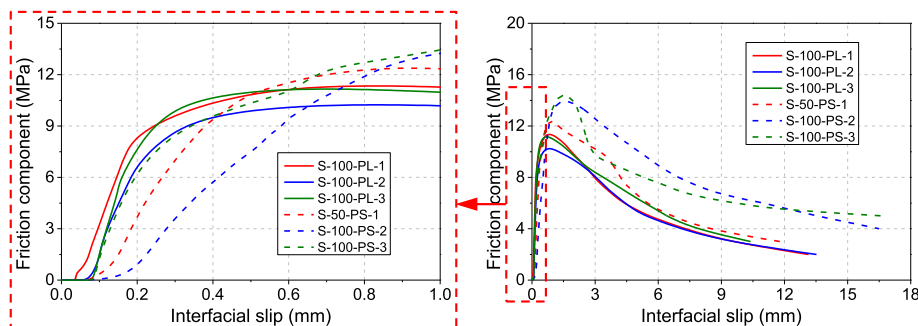


Fig. 15. Variation of the evaluated friction component with the interfacial slip.

For concrete under uniaxial tension, the tension-softening curve model by Hordijk [52] has been successfully used by researchers. This model is adopted in this paper,

$$\frac{\sigma_t}{f_t} = \left[1 + \left(c_1 \frac{w_t}{w_{cr}} \right)^3 \right] e^{-c_2 \frac{w_t}{w_{cr}}} - \frac{w_t}{w_{cr}} (1 + c_1^3) e^{-c_2} \quad (8)$$

$$w_{cr} = 5.14 \frac{G_f}{f_t} \quad (9)$$

where σ_t is the tensile stress; w_t is the crack opening displacement; w_{cr} is the crack opening displacement at the complete release of stress or fracture energy; $c_1 = 3.0$, $c_2 = 6.93$. f_t is the tensile strength and G_f is the fracture energy of concrete,

$$f_t = 1.4 \left(\frac{f'_{co} - 8}{10} \right)^{2/3} \quad (10)$$

$$G_f = \gamma \left(\frac{f'_{co}}{10} \right)^{0.7} \quad (11)$$

where γ is 0.03 for normal aggregate concrete.

In all the FE models, lateral displacements were uniformly imposed on the concrete surface within the bond zone. The nonlinear geometry NLGEOM option in ABAQUS was turned on for all the analysis.

A mesh sensitivity analysis was firstly conducted considering three levels of mesh with approximate sizes of 10 mm, 15 mm and 20 mm. The frictionless and tie option in ABAQUS are adopted for concrete-tube interface. The obtained interfacial dilatation-pressure and interfacial dilatation-hoop strain relationships are shown in Fig. 17. It can be seen that the selected element sizes yield very close results. In the present paper, an element size of 10 mm for both concrete and FRP tube was adopted.

The influence of concrete-tube interfacial configuration on the numerical results was examined. The investigated interfaces include tie, frictionless, and friction with a penalty coefficient varying from 0.2 to 0.8. For frictionless and friction behavior in the tangential direction, hard contact was adopted for the normal behavior. As shown in Fig. 18, the tangential behavior of the interface shows some influence on the interfacial dilatation-pressure relationship. The tie connection leads to the upper limit of interfacial pressure, while the frictionless contact leads to the lower limit. The difference between the upper limit and the lower limit is insignificant until very large interfacial dilatation. For tangential behavior with penalty friction coefficient larger than 0, the interfacial pressure is intermediate between the upper limit and the lower limit. For the interfacial dilatation-hoop strain relationship, the interface parameter has very limited influence. In the present paper, the maximum dilatation is less 0.3 mm and the tie connection is adopted as it is easier to get convergent analysis.

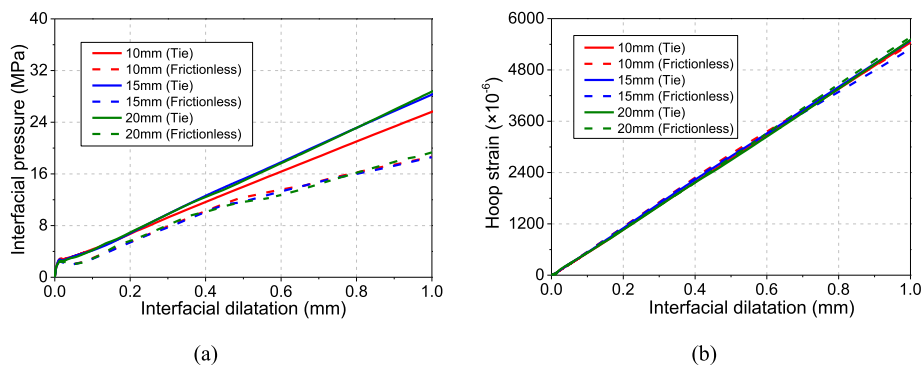


Fig. 17. Influence of mesh size on the numerical results: (a) the interfacial dilatation-pressure relationship; (b) the interfacial dilatation-hoop strain relationship.

In the experimental tests, the interfacial dilatation was activated by the shear behavior in the longitudinal direction. The interfacial pressure was coupled with the shear stress at the plate-concrete interface. Therefore, shear stress with varying levels in the longitudinal direction was also applied at the bonding interface together with the displacement loads. As shown in Fig. 19, the applied shear stress shows a clear influence on the interfacial dilatation-pressure and interfacial dilatation-hoop strain relationships. With the increase of shear stress, larger interfacial pressure as well as hoop strain is generated under the same dilatation.

To examine the influence of concrete model on numerical results, FE models based on CDP model and MCDP model are created and compared. For MCDP model, models by Teng et al. [51] and Yang and Feng [9] are respectively selected to generate the stress-strain data for concrete under compression. The mesh size is 10 mm, the concrete-tube interface is “tie”, and the shear stress applied at the interface are 0 MPa and 10 MPa. Fig. 20 shows the numerical results based on different concrete models. Apparently, the numerical results based on Teng et al. [51] model and Yang and Feng [9] model are almost the same. This indicates that the confinement condition in the present study can be classified as weak or moderate. Compared with CDP model, MCDP model do yield different numerical results, particularly the interfacial dilatation-pressure relationship. However, the difference is negligible until very large interfacial dilatation (larger than 0.2 mm) is developed. As the maximum interfacial dilatation is less than 0.2 mm in this study, the above three models can lead to very close numerical results. Therefore, any of them can be selected for FE analysis.

Fig. 21 shows the cracking patterns of concrete block obtained from FE analysis. PEEQT, which is the equivalent plastic strain in uniaxial tension, is selected for representing concrete cracking. According to FE analysis, serious concrete cracking takes place at the right and left side of FRP plate, and both horizontal and inclined cracks are formed. In general, the calculated concrete cracking patterns are consistent with experimental observations. This demonstrates that the interfacial dilatation effect can be well simulated by the 3D FE model.

Using the measured hoop strains of each specimen, the development of the interfacial dilatation and the interfacial pressure can be determined through interpolation based on Fig. 19. The obtained interfacial dilatation-slip curves are shown in Fig. 22(a). It can be seen that the interfacial dilatation increases with the slip initially, and after reaching the peak the dilatation begins to decrease gradually. The initial increase of dilatation with slip is because the roughness asperities ride on top of each other, while the gradual decrease after the peak is due to the gradually accumulated interfacial damage. The fundamental mechanism that drives the interfacial dilatation is the mechanical interlock between fractured concrete surfaces. Therefore, the interfacial slip-dilatation relationship might be related to hoop confinement

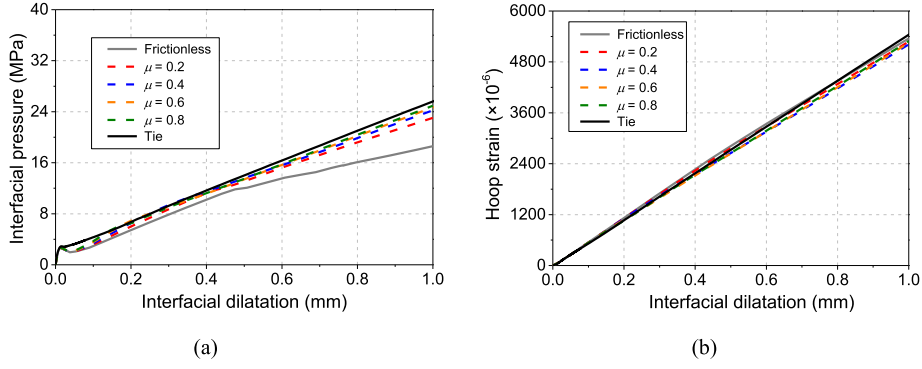


Fig. 18. Influence of FRP tube-concrete interface on the numerical results: (a) the interfacial dilatation-pressure relationship; (b) the interfacial dilatation-hoop strain relationship.

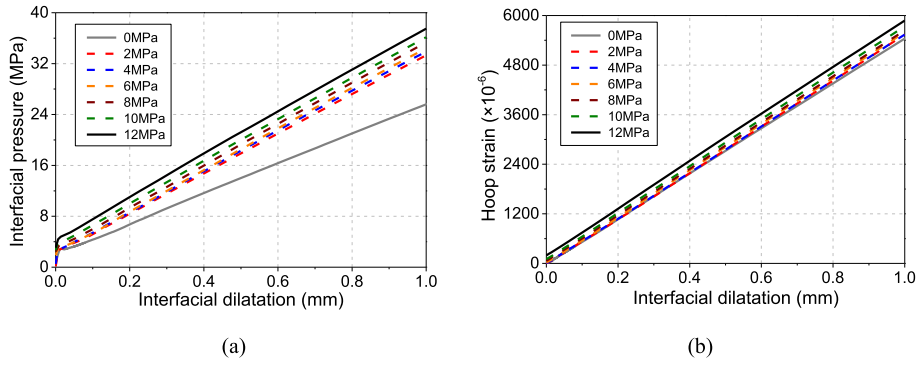


Fig. 19. Influence of interfacial shear stress on the numerical results: (a) the interfacial dilatation-pressure relationship; (b) the interfacial dilatation-hoop strain relationship.

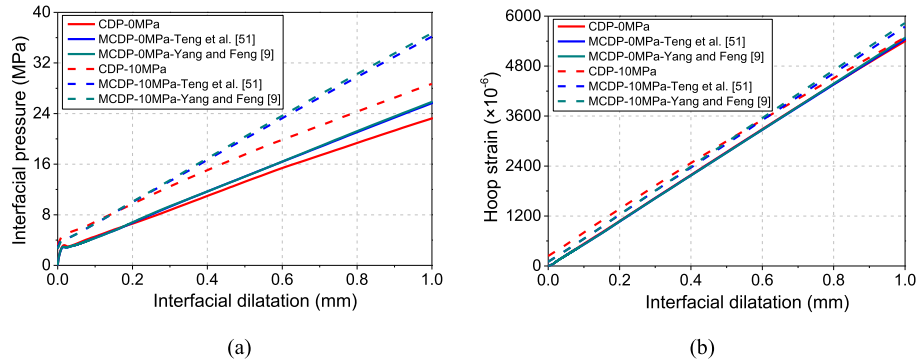


Fig. 20. Influence of concrete model on the numerical results: (a) the interfacial dilatation-pressure relationship; (b) the interfacial dilatation-hoop strain relationship.

stiffness and concrete properties. However, no relevant test data can be found in the literature right now. As a compromise, this study only focus on the relationship between the interfacial slip and the lateral dilatation. This does not affect the accuracy of the conclusions of the present study, and it only limits the application of the proposed interface model. In a parallel study by the authors, the influence of lateral confinement stiffness on the interfacial dilatation relationship will be discussed. With proper interfacial slip-dilatation relationship in the future, the proposed bond model in this paper can be updated. To better understand the interfacial slip-dilatation relationship, all the tested curves were normalized, see Fig. 22(b). As can be seen, the data scatter is much reduced. The following equation is utilized to describe the interfacial slip-dilatation relationship,

$$\delta = 0 \quad (0 \leq s \leq s_{cs}) \quad (12a)$$

$$\frac{\delta}{\delta_{max}} = \frac{s - s_{cs}}{s_{\delta_{max}} - s_{cs}} \frac{k_{\delta_1}}{k_{\delta_1} - 1 + \left(\frac{s - s_{cs}}{s_{\delta_{max}} - s_{cs}}\right)^{k_{\delta_1}}} \quad (s_{cs} < s) \quad (12b)$$

where δ_{max} and $s_{\delta_{max}}$ are the maximum interfacial dilatation and corresponding slip, respectively; δ is the lateral dilatation; k_{δ_1} is an empirical parameter; s_{cs} is the critical slip introduced in Eq. (2). In average, δ_{max} and $s_{\delta_{max}}$ can be taken as 0.188 mm and 4.00 mm, respectively. By means of regression analysis, the value of k_{δ_1} is 1.49. Fig. 23 shows the comparisons between the test data and the predictions by Eq. (12). The fitted curve agrees very well with the test results.

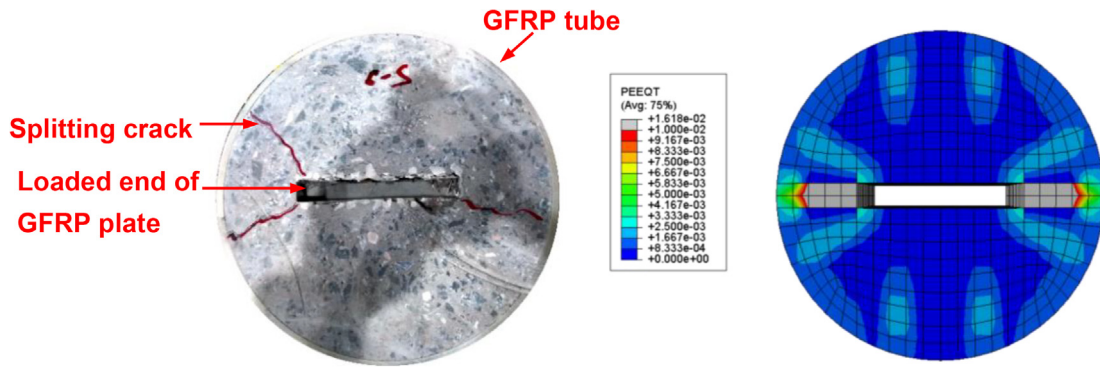


Fig. 21. Comparisons between tested and FE predicted concrete cracking patterns.

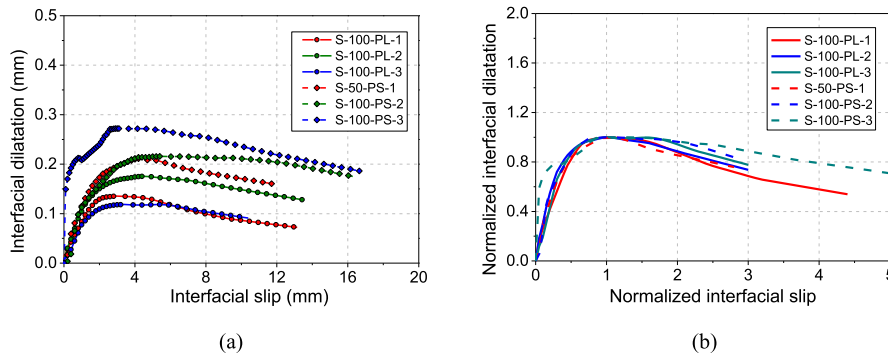


Fig. 22. Variation of the interfacial dilatation with the interfacial slip: (a) tested curves; (b) normalized curves.

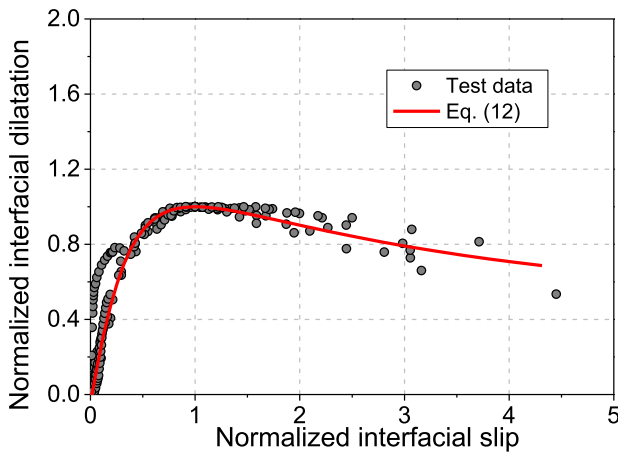


Fig. 23. Comparisons between tested and predicted interfacial dilatation.

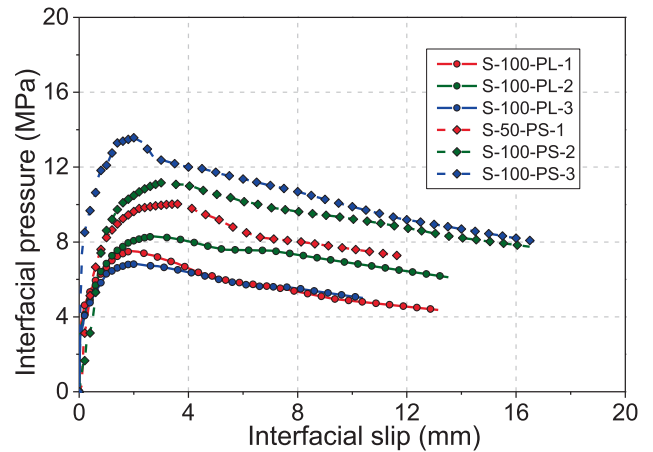


Fig. 24. Development of the interfacial pressure with the interfacial slip.

As mentioned above, the interfacial pressure can be obtained based on tested curves and Fig. 19, see Fig. 24. Like the interfacial dilatation, the interfacial pressure increased firstly to the peak and then decreased gradually. According to the friction law, the interfacial friction is proportion to the interfacial pressure,

$$\tau_f(s) = \mu(s)\sigma_{ip}(s) \quad (13)$$

For passive confinement,

$$\sigma_{ip}(s) = K_{inp}(s)\delta \quad (14)$$

where $\mu(s)$ is the friction coefficient; $\sigma_{ip}(s)$ is the interfacial pressure; $K_{inp}(s)$ is the lateral confinement stiffness; δ is the lateral dilatation (Eq. 12). With the estimated friction component of each specimen in Fig. 15, the development of friction coefficient can be obtained using Eq. (13), see Fig. 25.

With the increase of interfacial slip, the friction coefficient increases initially and then attenuates gradually. The reason for this phenomenon is also due to the gradually accumulated interfacial damage. It should be noticed that the calculated friction coefficient is neg-

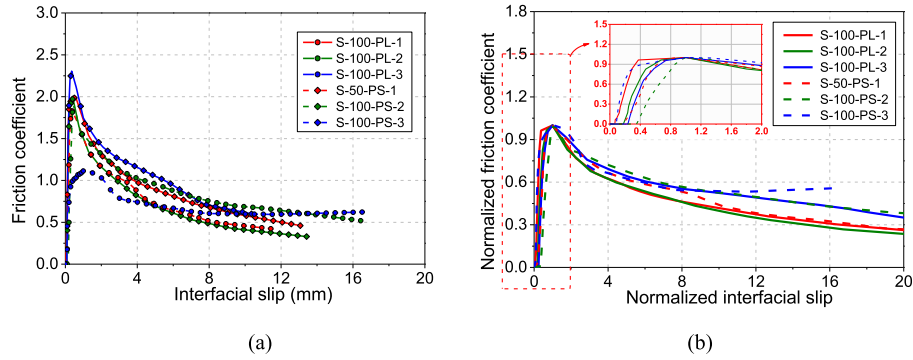


Fig. 25. Variation of the interfacial friction coefficient with the interfacial slip: (a) calculated values; (b) normalized curves.

active or zero prior to the slip value varying from 0.04 mm to 0.08 mm. This indicates that friction action is hardly activated in the initial stage. To reduce the influence of data scatter and better understand the development of the friction coefficient, the curves in Fig. 25(a) are normalized, see Fig. 25(b). The following equation is selected to describe the development of friction coefficient with the slip,

$$\frac{\mu(s)}{\mu_{\max}} = \frac{s}{s_{\mu_{\max}}} \frac{k_{\mu 1}}{k_{\mu 1} - 1 + \left(\frac{s}{s_{\mu_{\max}}}\right)^{k_{\mu 1}}} \quad (15)$$

where μ_{\max} and $s_{\mu_{\max}}$ are the maximum friction coefficient and corresponding slip, and they can be taken as 2.00 and 0.40 mm, respectively; the empirical parameter $k_{\mu 1}$ is 1.58 through regression analysis. Fig. 26 shows the comparisons between tested data and fitting curve. As can be seen, the fitting curve agrees very well with the test results.

4.3. Pressure-dependent bond stress-slip model

Substituting Eq. (2) and Eq. (13) into Eq. (3), the interfacial bond stress-slip relationship model for sand-coated FRP-concrete interface is established,

$$\tau(s) = 4\tau_{cs}(e^{-k_{cs}s} - e^{-2k_{cs}s}) + \mu(s)\sigma_{ip}(s) \quad (16)$$

where the friction coefficient $\mu(s)$ can be evaluated by Eq. (15); the interfacial pressure, $\sigma_{ip}(s)$, is related to the lateral confinement, see Eq. (14).

In the development of the above bond-slip model, the test data of short bond length specimens were utilized. Normally, the model

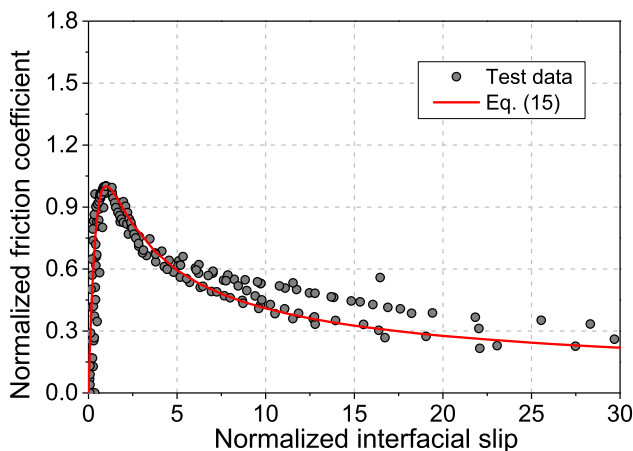


Fig. 26. Comparisons between test data and predictions by Eq. (15).

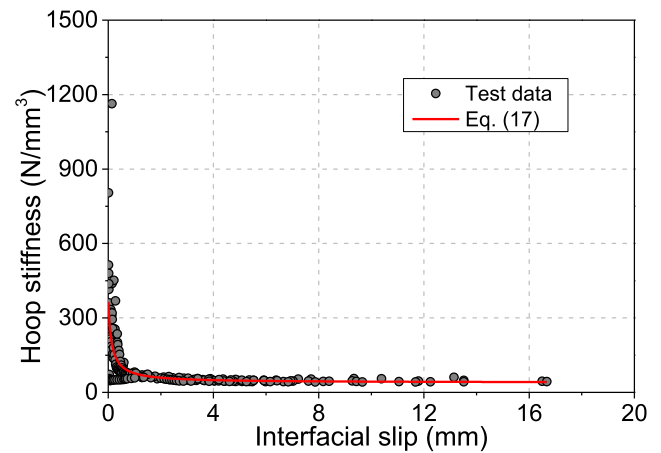


Fig. 27. Interfacial confinement stiffness of the short bond length specimens.

should be self-consistent, i.e. the model should fit well with the test data of short bond length specimens. According to the derived interfacial dilatation in Fig. 22(a) and interfacial pressure in Fig. 24, the passive confinement stiffness of each specimen, i.e. the ratio of interfacial pressure to interfacial dilatation, can be obtained (see Fig. 27). Through regression analysis, the interfacial stiffness is approximated by the following equation,

$$K_{int} = \frac{s + 1.22}{0.0256s + 0.0032} \quad (17)$$

Combining Eqs. (13), (14) and (16), the theoretical bond stress-slip relationship can be obtained. The predicted curves are compared with the tested curves in Fig. 28. Both the predicted bond stress-slip behavior and the interfacial dilatation agree very well with the test results.

4.4. Model performance under different confinement conditions

Based on Eq. (16), the local bond stress-slip relationships under active and passive confinement conditions are discussed. All the material parameters are based on the present paper. Since the problem analyzed in this paper contains four variables, i.e. $(\tau, s, \sigma_{ip}, \delta)$, the stress-slip model can be interpreted in a 3-dimensional manner as shown in Fig. 29. In the 3-dimensional plot, the geometrical meanings of the model as well as different loading cases can be expressed intuitively. Details of the 3D interpretation of four-variable functions can be found in Yang and Feng [9]. Fig. 29(a) shows the influence of constant lateral pressure on the bond stress-slip relationship. The bond stress increases with the slip to the peak with a very steep slope and then drops rapidly. Fig. 29(b) shows the bond stress-slip curves under varying pas-

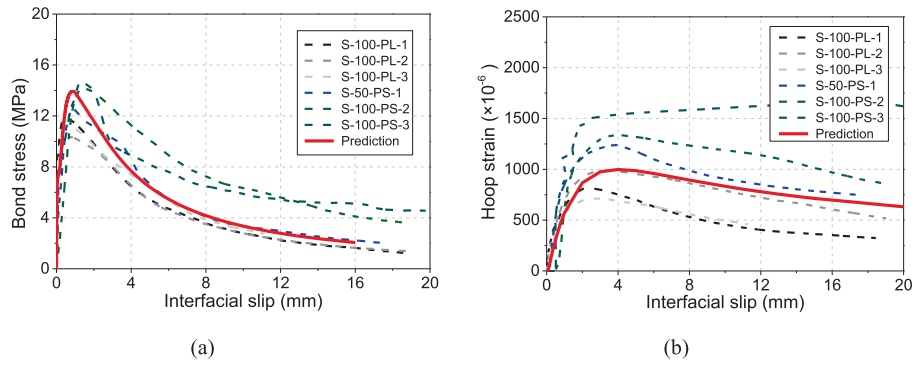


Fig. 28. Comparisons between model predictions and test results of short bond length specimens: (a) bond stress-slip curves; (b) hoop strain.

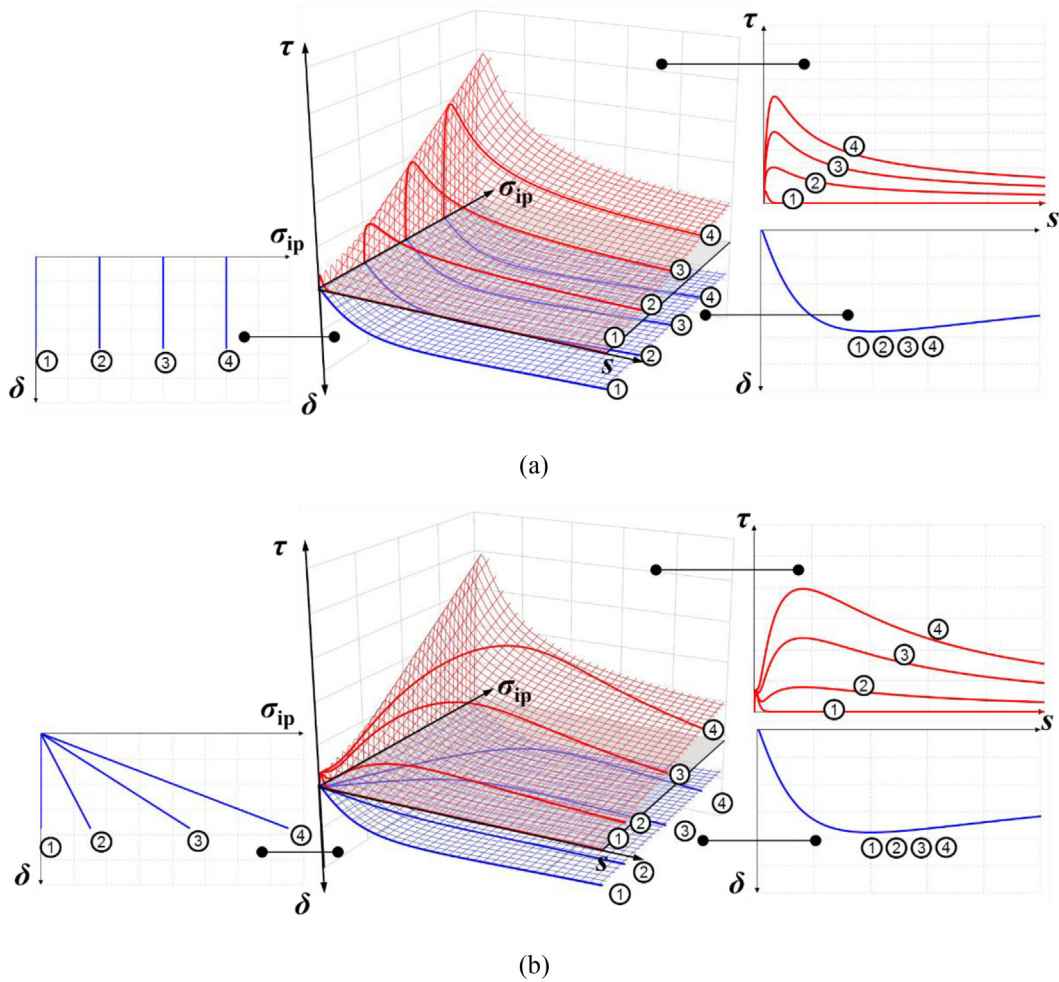


Fig. 29. Bond stress-slip curves with lateral confinements: (a) active confinement; (b) passive confinement.

sive confinement levels. The bond behavior under passive confinement is different with that under active confinement. When the lateral confinement stiffness is relatively low, two peaks for the curves can be observed. The first peak is associated with concrete shear behavior. After the first peak, there is a sharp drop of the bond stress due to concrete cracking. Simultaneously, the friction behavior takes place at the interface and the friction increases with the slip to the second peak. When the lateral confinement stiffness is relatively large, the bond loss due to concrete cracking will be compensated by the friction and only one peak will be observed (curve ④). Compared with the condition

when no lateral confinement is present, the actively and passively confined specimens show much better interfacial behavior. The interfacial strength, stiffness and ductility are significantly improved.

5. Model verification

5.1. Comparisons with test results in the literature

To have a further understanding of the proposed model, literature studies are selected for comparisons. For FRP-concrete interface with-

out lateral confinement, numerous studies are available in the literature and many models for the interfacial loading capacity have been proposed. Among the strength models, the most widely accepted one is the one proposed by Chen and Teng [53]. After an assessment of existing anchorage strength models for FRP-concrete bonded joints under shear, they proposed a new model based on fracture mechanics analysis and experimental observations. This model agrees very well with test data gathered from the literature. For FRP-concrete joint under shear, the anchorage strength model is formulated as follows,

$$P_u = 0.427\beta_w\beta_L\sqrt{f'_c}b_fL_e \quad (18)$$

where β_w is the width ratio factor, $\beta_w = \sqrt{\frac{2-b_f/b_c}{1+b_f/b_c}}$, b_c is the width of concrete prism, b_f is the width of FRP plate; L_e is the effective bond length, $L_e = \sqrt{\frac{E_f t_f}{\sqrt{f'_c}}}$, t_f and E_f are the thickness and Young's modulus of the bonded FRP plate, respectively; β_L is the bond length factor, β_L is 1.0 when bond length L is larger than L_e and $\beta_L = \sin \frac{\pi L}{2L_e}$ when L is smaller than L_e .

Based on this anchorage strength model, the local maximum bond stress for FRP-concrete interface without lateral confinement can be obtained when the bond length tends to 0,

$$\tau_{max} = \lim_{L \rightarrow 0} \frac{P_u}{b_f L} = \lim_{L \rightarrow 0} \frac{0.427\beta_w\sqrt{f'_c}L_e}{L} \sin \frac{\pi L}{2L_e} = 0.67\beta_w\sqrt{f'_c} \quad (19)$$

In Fig. 30, the predicted maximum bond stress by Eq. (16) are compared with those by Eq. (19). For different concrete classes, the values suggested by Eurocode 2 [54] for concrete compressive and tensile strength are adopted. When no lateral pressure is present, the maximum bond stress increases almost linearly with the concrete compressive strength and the predictions by both equations are very close. With the increase of lateral pressure, the influence of concrete strength on the bond strength becomes insignificant.

Until now, studies on the interfacial behavior of FRP-concrete interface under active confinement are limited. Direct comparisons between the proposed model and test data is yet impossible. Biscaia et al. [41] conducted a preliminary study on the bond behavior of GFRP-concrete adhesive-bonding interface under lateral compression. The adopted lateral pressure were 0.5 MPa, 1 MPa and 2 MPa. The friction angle of GFRP-concrete adhesive-bonding interface for different concrete strengths were indirectly derived. Although the interface in their tests is different with the present study, similarities exist in regard to the failure mode. Their test results are therefore selected for a reference. Table 4 lists the tested and predicted friction angle of specimens with cohesive failure mode. As can be seen, the friction

angles are slightly underestimated by Eq. (16) with an overall error of -20% . Considering the considerable difference in material properties and loading tests, the deviation is conservative and acceptable.

5.2. Comparisons with test results of the specimen L-250-PL

To verify the effectiveness when the model is used for structural members, the test data of the long bond length specimen L-250-PL is selected for comparison. A 3D FE model of specimen L-250-PL was created by ABAQUS, as shown in Fig. 31. Only a quarter of the specimen was modeled. The concrete block, and the FRP plate were meshed with solid elements C3D8R. The FRP jacket was meshed with membrane elements M3D4R. The plate-concrete interface was modeled by 8-node cohesive elements (COH3D8) with a thickness of 1.0 mm. For the concrete-tube interface, hard contact in the normal direction and frictionless in the tangential direction were adopted. The adopted mesh size for all the elements was 10 mm.

Concrete damage plasticity model was adopted for the concrete material. The FRP plate was treated as an anisotropic material defined by engineering constants in ABAQUS. The FRP tube was all modeled as elastic material. The proposed bond model was implemented into ABAQUS by means of the user-defined subroutine USDFLD. The interfacial dilatation effect was modeled by the expansion of the cohesive elements. The association of the normal expansion with the shear displacements of the cohesive elements was defined through the "field expansion" option in ABAQUS. Details about the modelling techniques will be reported elsewhere.

Fig. 32 shows the comparisons between numerical results and test results. Prior to the plate failure at the loading point, the predicted load-displacement curves agree fairly well with the tested curves. Both the displacements at the load-end and the free-end are well estimated. In the loading test of specimen L-250-PL, the tensile strains of FRP plate at different locations of the bond length were monitored. As shown in Fig. 32(b), the developments of the tensile strains at locations 190 mm, 160 mm and 90 mm are well predicted. The tensile strains at locations 60 mm and 30 mm are overestimated. The possible reason for the overestimation might be due to the data scatter. Because the measured strains were small in magnitude and they could be easily affected by experiment-related data errors. Another reason is that the continuous FRP-concrete interface is divided into discrete cohesive elements with a size of 10 mm. For refined results, a smaller element size should be adopted. For the hoop strains of GFRP tube, the predictions are also reasonable. In general, the mechanical behavior of the specimen L-250-PL can be well approximated with the proposed bond model.

6. Conclusion

This paper deals with the interfacial behavior between sand-coated FRP profile and concrete under lateral confinement. Based on test results and numerical analysis, the following conclusions can be drawn:

- (1) For the investigated interface in this study, the failure firstly occurred in the concrete surrounding the plate. Afterwards, the sand-adhesive interface and the plate-adhesive interface were damaged due to significant friction.
- (2) With lateral confinement the interfacial behavior of the sand-coated FRP-concrete interface includes two stages: stage I and stage II. In stage I the interfacial behavior is characterized by concrete shear; in stage II, interfacial dilatation takes place and the friction between fractured surfaces of concrete becomes dominant.

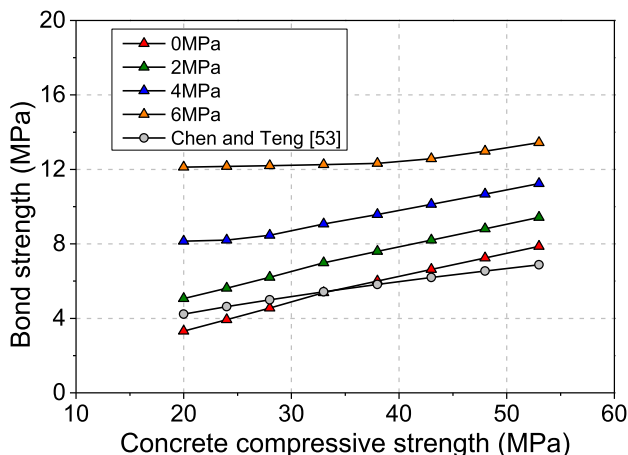


Fig. 30. Comparisons with the strength model by Chen and Teng [53].

Table 4
Comparisons with the literature data in [41].

Designation	f'_{co} (MPa)	f_t (MPa)	σ_{ip} (MPa)	Tested friction angle (rad)	Predicted friction angle (rad)	Error (%)
MC1-C1	14.9	1.47	0.5	0.90	0.7652	-14.97
MC1-C2			1	1.00		-23.48
MC2-C1	34.9	2.95	0.5	1.00	0.7631	-23.69
MC2-C2			1.0	1.05		-27.32
MC2-C3			2.0	0.87		-12.28

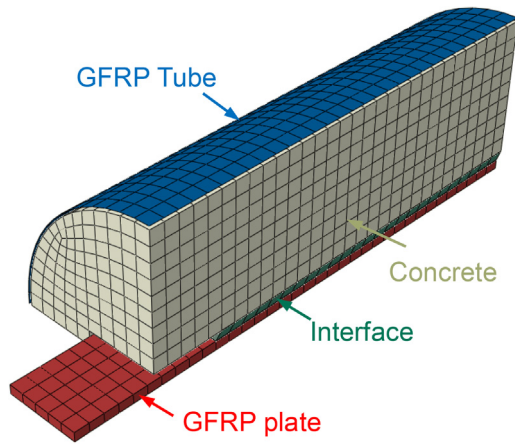


Fig. 31. 3D FE model of the pullout specimen L-250-PL.

(3) In the first stage, the interfacial behavior can be well described by previous models for externally bonded FRP joint. In the second stage, the interfacial dilatation and the friction coefficient increase firstly and then decreases gradually with the increase

of slip. Based on the above knowledge, a pressure-dependent bond stress-slip model for sand-coated FRP-concrete interface is developed.

- (4) Both active and passive confinement can significantly improve the mechanical behavior of FRP-concrete interface.
- (5) A user-defined subroutine program is developed for the proposed bond stress-slip model. With the subroutine program, the model can be implemented into commercial FE software and used for structural analysis.

CRedit authorship contribution statement

Hongwei Lin: Conceptualization, Data curation, Formal analysis, Investigation, Methodology, Writing - review & editing. **Peng Feng:** Conceptualization, Resources, Funding acquisition, Project administration, Writing - review & editing, Supervision. **Jia-Qi Yang:** Investigation, Methodology.

Declaration of Competing Interest

The authors declare that they have no known competing financial interests or personal relationships that could have appeared to influence the work reported in this paper.

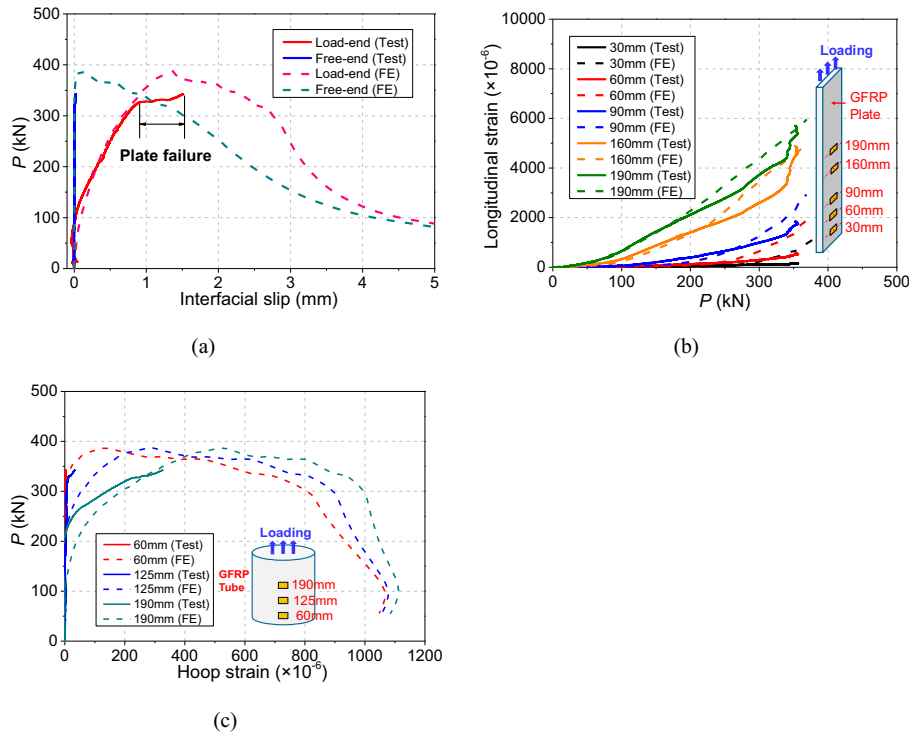


Fig. 32. Comparisons between numerical results and test data of specimen L-250-PL: (a) load-displacement curve; (b) tensile strain of FRP plate; (c) hoop strain of GFRP tube.

Acknowledgements

This work was supported by the National Key Research and Development Program of China (No. 2017YFC0703000), the China Postdoctoral Science Foundation Grant (No. 2018M630163), China Postdoctoral Science Special Foundation Grant (No. 2019 T120096), and the National Natural Science Foundation of China (No. 51978379).

References

- Stewart MG, Wang XM, Nguyen MN. Climate change adaptation for corrosion control of concrete infrastructure. *Struct Saf* 2012;35(1):29–39.
- Ožbolt J, Oršanić F, Balabanić G. Modelling processes related to corrosion of reinforcement in concrete: coupled 3d finite element model. *Struct Infrastruct Eng* 2017;13(1):135–46.
- Li M, Ranade R, Kan L, Li VC. On improving the infrastructure service life using ECC to mitigate rebar corrosion. In: *2nd International Symposium on Service Life Design for Infrastructures*. p. 773–81.
- Lin H, Zhao Y, Feng P, Ye H, Ožbolt J, Jiang C, et al. State-of-the-art review on the bond properties of corroded reinforcing steel bar. *Constr Build Mater* 2019;213:216–33.
- Hou B, Li X, Ma X, Du C, Zhang D, Zheng M, et al. The cost of corrosion in China. 2017;1(1). <https://doi.org/10.1038/s41529-017-0005-2>.
- Mirmiran A, Shahawy M. Fiber reinforced plastic (“FRP”)–concrete composite structural members. US Patents, 1997, No 5599599A.
- Park JS, Lee SS, Nam JH, Kang IK, An DJ, Yoon SJ. Load carrying capacity of hybrid FRP-concrete composite pile. *Adv Mater Res* 2011;250-253:1165–72.
- Wang J. Structural behaviors of PPR-CFFT column and joint for ocean construction PhD thesis. Beijing, China: Tsinghua University; 2018.
- Yang JQ, Feng P. Analysis-oriented models for FRP-confined concrete: 3d interpretation and general methodology. *Eng Struct* 2020;216(1):110749.
- Yuan JS, Hadi MNS. Bond-slip behaviour between GFRP I-section and concrete. *Compos B Eng* 2017;130(1):76–89.
- Yuan JS, Hadi MN. Friction coefficient between FRP pultruded profiles and concrete. *Mater Struct* 2018;51(1):1–10.
- Bank LC, Oliva MG, Bae H-U, Barker JW, Yoo S-W. Pultruded FRP plank as formwork and reinforcement for concrete members. *Adv Struct Eng* 2007;10(5):525–35.
- Shao Y, Wu ZS, Bian J. Wet-Bonding between FRP Laminates and Cast-in-Place Concrete. In: *Proceedings of the International Symposium on Bond Behaviour of FRP in Structures (BFS 2005)*. Hong Kong, 2005. p. 91–96.
- Zhang L, Wang W-W, Harries KA, Tian J. Bonding behavior of wet-bonded GFRP-concrete interface. *J Compos Constr* 2015;19(6):04015001. [https://doi.org/10.1061/\(ASCE\)CC.1943-5614.0000550](https://doi.org/10.1061/(ASCE)CC.1943-5614.0000550).
- Zhang Pu, Wu G, Zhu H, Meng S-P, Wu Z-S. Mechanical performance of the wet-bond interface between FRP plates and cast-in-place concrete. *J Compos Constr* 2014;18(6):04014016. [https://doi.org/10.1061/\(ASCE\)CC.1943-5614.0000472](https://doi.org/10.1061/(ASCE)CC.1943-5614.0000472).
- Cho J-R, Cho K, Park SY, Kim ST, Kim B-S. Bond characteristics of coarse sand coated interface between stay-in-place fibre-reinforced polymer formwork and concrete based on shear and tension tests. *Can J Civil Eng* 2010;37(5):706–18.
- Honickman H, Nelson M, Fam A. Investigation into the bond of glass fibre-reinforced polymer stay-in-place structural forms to concrete for decking applications. *Trans Res Rec* 2009;2131:134–44.
- Goyal R, Mukherjee A, Goyal S. An investigation on bond between frp stay-in-place formwork and concrete. *Constr Build Mater* 2016;113(1):741–51.
- Zhang Pu, Liu H, Gao D, Zhao J, Feng Hu, Tang G. Shear-bond behavior of the interface between FRP profiles and concrete by the double-lap push shear method. *J Compos Constr* 2017;21(4):04017012. [https://doi.org/10.1061/\(ASCE\)CC.1943-5614.0000795](https://doi.org/10.1061/(ASCE)CC.1943-5614.0000795).
- Zhang Pu, Zhu H, Wu G, Meng S-P, Wu Z-S. Shear capacity comparison of four different composite interfaces between FRP plates and concrete substrate. *J Compos Constr* 2016;20(4):04016006. [https://doi.org/10.1061/\(ASCE\)CC.1943-5614.0000666](https://doi.org/10.1061/(ASCE)CC.1943-5614.0000666).
- Correia JR, Branco FA, Ferreira JG. Flexural behaviour of GFRP-concrete hybrid beams with interconnection slip. *Compos Struct* 2007;77(1):66–78.
- Kwan WH, Ramli M. Indicative performance of fiber reinforced polymer (FRP) encased beam in flexure. *Constr Build Mater* 2013;48:780–8.
- Neaogoe CA, Gil L, Pérez MA. Experimental study of GFRP-concrete hybrid beams with low degree of shear connection. *Constr Build Mater* 2015;101:141–51.
- Nordin H, Täljsten B. Testing of hybrid FRP composite beams in bending. *Compos Part B Eng* 2004;35(1):27–33.
- Zou XX, Feng P, Wang JQ. Perforated FRP ribs for shear connecting of FRP-concrete hybrid beams/decks. *Compos Struct* 2016;152:267–76.
- El-Hacha R, Chen D. Behaviour of hybrid FRP-UHPC beams subjected to static flexural loading. *Compos Part B Eng* 2012;43(2):582–93.
- Fam A, Skutezky T. Composite T-beams using reduced-scale rectangular FRP tubes and concrete slabs. *J Compos Constr* 2006;10(2):172–81.
- Nguyen H, Mutsuyoshi H, Zatar W. Push-out tests for shear connections between UHPFRC slabs and FRP girder. *Compos Struct* 2014;118:528–47.
- Lameiras R, Valente IB, Barros JAO, Azenha M, Gonçalves C. Pull-out behaviour of glass-fibre reinforced polymer perforated plate connectors embedded in concrete. Part I: experimental program. *Constr Build Mater* 2018;162:155–69.
- Lameiras R, Barros JAO, Valente IB, Xavier J, Azenha M. Pull-out behaviour of glass-fibre reinforced polymer perforated plate connectors embedded in concrete. Part II: prediction of load carrying capacity. *Constr Build Mater* 2018;169:142–64.
- Lameiras R, Barros J, Valente IB, Azenha M. Development of sandwich panels combining fibre reinforced concrete layers and fibre reinforced polymer connectors. Part I: conception and pull-out tests. *Compos Struct* 2013;105:446–59.
- Gai X, Darby A, Ibell T, Evernden M. Experimental investigation into a ductile FRP stay-in-place formwork system for concrete slabs. *Constr Build Mater* 2013;49(12):1013–23.
- Xiong Z, Liu Y, Zuo Y, Xin H. Experimental evaluation of shear behavior of pultruded GFRP perforated connectors embedded in concrete. *Compos Struct* 2019;222:110938. <https://doi.org/10.1016/j.compstruct.2019.110938>.
- Cho K, Cho J-R, Chin W-J, Kim B-S. Bond-slip model for coarse sand coated interface between FRP and concrete from optimization technique. *Comput Struct* 2006;84(7):439–49.
- Cho K, Park SY, Kim ST, Cho J-R, Kim B-S. Freeze-thaw effect on coarse sand coated interface between FRP and concrete. *Eng* 2013;05(10):807–15.
- Lee J, Lopez MM. Frictional bond-slip model for the concrete-FRP interface under the FRP U-wrap region. *Constr Build Mater* 2019;194(1):226–37.
- Lee J, Lopez MM. Characterization of FRP Uwrap anchors for externally bonded FRP-reinforced concrete elements: an experimental study. *J Compos Constr* 2016;20(4):04016012. [https://doi.org/10.1061/\(ASCE\)CC.1943-5614.0000642](https://doi.org/10.1061/(ASCE)CC.1943-5614.0000642).
- Zhou Y, Wang X, Sui L, Xing F, Huang Z, Chen C, et al. Effect of mechanical fastening pressure on the bond behaviors of hybrid-bonded FRP to concrete interface. *Compos Struct* 2018;204:731–44.
- Wu Y-F, Liu K. Characterization of mechanically enhanced FRP bonding system. *J Compos Constr* 2013;17(1):34–49.
- Biscaia HC, Chastre C, Silva MAG. Bond-slip model for FRP-to-concrete bonded joints under external compression. *Compos Part B Eng* 2015;80(1):246–59.
- Biscaia HC, Chastre C, Silva MAG. Double shear tests to evaluate the bond strength between GFRP/concrete elements. *Compos Struct* 2012;94(2):681–94.
- Lin HW, Zhao YX, Ožbolt J, Feng P, Jiang C, et al. Analytical model for the bond stress-slip relationship of deformed steel bars. *Constr Build Mater* 2016;198:570–86.
- Abaqus v6.14. ABAQUS Analysis User's manual. Dassault Systemes Simulia Corp; 2014.
- Nakaba K, Kanakubo T, Furuta T, Yoshizawa H. Bond behavior between fiber-reinforced polymer laminates and concrete. *ACI Struct J* 2001;98(3):359–67.
- Dai J, Ueda T, Sato Y. Development of the nonlinear bond stress-slip model of fiber reinforced plastics sheet-concrete interfaces with a simple method. *J Compos Constr* 2005;9(1):52–62.
- Lu XZ, Teng JG, Ye LP, Jiang JJ. Bond-slip models for FRP sheets/plates bonded to concrete. *Eng Struct* 2005;27(6):920–37.
- Lubliner J, Oliver J, Oller S, Ate O, E. A plastic-damage model for concrete. *Int J Solid Struct* 1989;25:299–329.
- Lee J, Fenves GL. Plastic-damage model for cyclic loading of concrete structures. *J Eng Mech* 1998;124(8):892–900.
- Yu T, Teng JG, Wong YL, Dong SL. Finite element modeling of confined concrete-II: plastic-damage model. *Eng Struct*;32(3):680-91.
- Yu T, Teng JG, Wong YL, Dong SL. Finite element modeling of confined concrete-I: drucker-prager type plasticity model. *Eng Struct* 2010;32(3):665–79.
- Teng JG, Huang YL, Lam L, Ye LP. Theoretical model for fiber-reinforced polymer-confined concrete. *J Compos Constr* 2007;11(2):201–10.
- Hordijk PA. Local approach to fatigue of concrete. Doctoral Thesis, Delft University, Netherland;1991.
- Chen JF, Teng JG. Anchorage strength models for FRP and steel plates bonded to concrete. *J Struct Eng* 2001;127(7):784–91.
- CEN. Eurocode 2: design of concrete structures - Part 1-1: general rules and rules for buildings. EN 1992-1-1. Brussels, Belgium: European Committee for Standardization; 2004.